J Mater Sci (2024) 59:19038–19056

Chemical routes to materials

Thermal decomposition temperature-dependent bonding performance of Ag nanostructures derived from metal–organic decomposition

Chuncheng Wang[1,2], Hiroaki Tatsumi[2], and Hiroshi Nishikawa[2,*]

[1] *Graduate School of Engineering, Osaka University, Suita 565-0871, Japan*
[2] *Joining and Welding Research Institute, Osaka University, Ibaraki 567-0047, Japan*

Received: 5 June 2024
Accepted: 18 September 2024
Published online: 15 October 2024

ABSTRACT

In wide-bandgap semiconductor power device packaging, die bonding refers to attaching the die to substrate. Thereby, the process temperature of Ag sintering for the die bonding should be low to prevent damage to fragile dies. Herein, an organic-free strategy using Ag nanostructures derived from the thermal decomposition of metal–organic decomposition (MOD) was proposed to achieve low-temperature bonding. Significant effects on bonding performance were determined by the thermal decomposition temperature, which in turn determined the organic content and sintering degree of Ag nanostructures. At a low thermal decomposition temperature of 160 °C, incomplete decomposition resulted in high organic content in the Ag nanostructures, causing large pores inside the Ag joints owing to the generation of gaseous products. Owing to the Ag particles with naked surfaces and wide size distribution, the Ag nanostructure obtained at 180 °C showed an excellent bonding performance, resulting in a high shear strength of 31.1 MPa at a low bonding temperature of 160 °C. As the thermal decomposition temperature was 200 °C, sintering among Ag particles increased the particle size, resulting in a reduction of surface energy and driving force for sintering. We think that uncovering this underlying mechanism responsible for the bonding performance will promote the application of Ag MOD in the die bonding of WBG power devices.

Handling Editor: Pedro Camargo.

Address correspondence to E-mail: nisikawa.jwri@osaka-u.ac.jp

https://doi.org/10.1007/s10853-024-10250-1

GRAPHICAL ABSTRACT

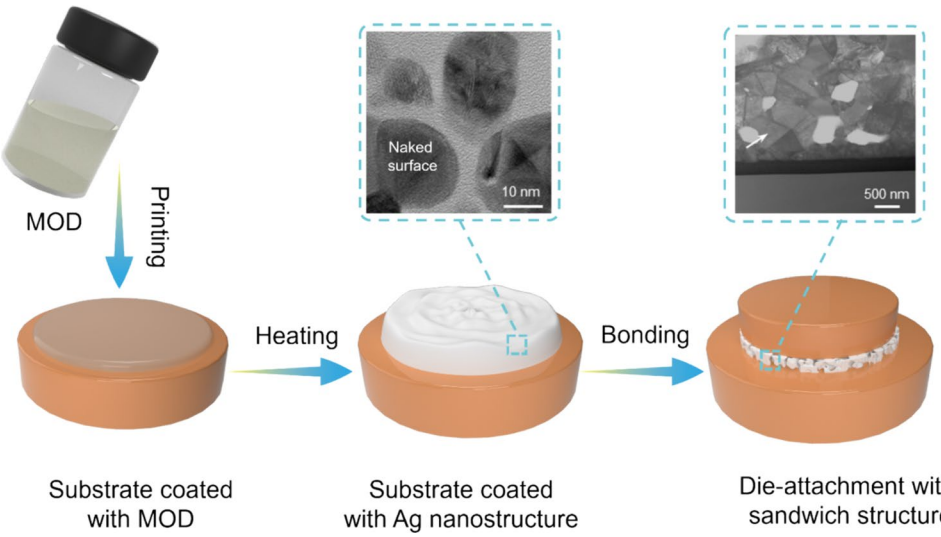

Introduction

Sintering is a long-standing technique for preparing ceramics and dates back to ancient times. Since the emergence of nanoscience and nanotechnology, sintering has become a research topic of significant scientific and technological importance [1]. Consequently, sintering has been widely used to prepare powder metallurgy, refractory materials, and high-temperature materials that have a broad range of applications in advanced technologies such as aerospace, electric vehicles (EV), and integrated circuits (IC) [2–5]. For example, bonding processes using Cu or Ag nanoparticle (NP) sintering, which provides reliable high-temperature die attachment, are becoming popular for replacing traditional soldering in the packaging of wide-bandgap (WBG) power devices [6–8]. Cu NP sintering is a cost-effective way to prepare high-temperature resistance for die attachment [9]. However, the poor oxidation resistance of Cu nanoparticles (NPs) tends to result in a Cu oxidation layer, which makes Cu atom diffusion difficult during the bonding processes [10]. Therefore, Ag NP sintering is an attractive and predominant method for preparing die attachments for WBG power devices.

Because multiple layers of different materials are stacked on top of dies, the mechanical stress induced by the coefficient of thermal expansion (CTE) mismatch tends to cause structural damage or failure of dies during bonding [11]. To prevent unexpected damage to dies, the processing temperature should be low to minimize mechanical stress. A convenient way to reduce the bonding temperature is to reduce the particle size and thus increase the surface-area-to-volume ratio and surface energy [12]. This is because the driving force for particle sintering is the reduction of surface energy [13]. For example, when the size is less than 20 nm, Ag NPs with a naked surface can automatically sinter into bulk Ag at room temperature [14]. However, Ag NPs with high surface energies are susceptible to van der Waals forces between NPs in close proximity, leading to the agglomeration of Ag NPs [15]. This agglomeration negatively affects the sintering of the Ag NPs by reducing the surface energy and destroying the uniformity of the Ag pastes [16]. Therefore, a complicated formula containing solvents, dispersants, and binders was designed to prevent the agglomeration of Ag NPs by reducing the surface energy and inducing steric and electrostatic stabilization [17]. However, dispersants and binders are prone to hinder atomic diffusion during the bonding process by forming an organic layer on the surface of Ag NPs, which increases the bonding temperature [18].

Several approaches have been proposed to eliminate the negative effects of organic additives such as using hybrid Ag powders and Ag particles with specific shapes, adding sintering aids, and optimizing

the bonding process [19–22]. For example, a shear strength of 42.3 MPa was achieved at 250 °C using a hybrid Ag powder containing submicron Ag particles and micron Ag flakes [23]. However, the enhancement effect of these methods is limited owing to the inevitable use of surface ligands such as dispersants and binders. Therefore, a new surface-ligand-free Ag sintering technique with excellent processability is required to achieve low-temperature Ag sintering.

To address these issues, Ag nanostructures derived from Ag metal–organic decomposition (MOD) were considered for creating sintered Ag joints in our previous study [24]. The Ag MOD was synthesized by the coordination reaction between silver acetate and 2-amino-2-methyl-1-propanol (AMP). The underlying mechanism responsible for the coordination reaction is that coordination bonds are easily formed between metal cations and ligands [25–28]. Coordination with organic ligands makes the metal precursor water-soluble, which increases the processability for printing and bonding [29]. In addition, the reductive ligands can reduce the metal cations at low temperatures, which allows the preparation of nanostructures without harming substrates or dies [30]. We successfully confirmed the feasibility of using Ag MOD as die attachment materials on Ag-plated direct-bonding copper (DBC) substrates in our previous study [24]. However, the effects of the processing temperature on the bonding performance of the Ag nanostructures and the Au-plated layer remain to be investigated.

In this study, the bonding performance of Ag nanostructures, derived at different temperatures, on Au was evaluated to optimize the application of MOD in the die-bonding process. The Ag nanostructures were directly created on the electroless nickel/immersion gold (ENIG) Cu substrates at 160 °C, 180 °C, and 200 °C and characterized by scanning electron microscopy (SEM) and transmission electron microscopy (TEM). Bonding of Ag nanostructures was conducted in a low-temperature range of 160–220 °C, and the shear strength of the sintered Ag joints was measured using die-shear tests. The sintering mechanism responsible for the low-temperature bonding was investigated by comprehensive SEM, energy-dispersive spectrometry (EDS), and TEM images of the fracture surface and cross section.

Materials and experimental procedure

Materials

Silver acetate (99%, FUJIFILM), 2-amino-2-methyl-1-propanol (AMP, FUJIFILM), and ethanol were purchased and used without further purification. ENIG Cu substrates were used as dummy dies ($D = 3$ mm) and dummy substrates ($D = 10$ mm). Before using the ENIG Cu substrates, possible surface impurities were removed by ultrasound in ethanol.

Synthesis of Ag MOD

For the synthesis of Ag MOD, a mixture of silver acetate and AMP in a 1:2 molar ratio was magnetically stirred in water for 30 min without exposure to light. Consequently, the solid silver acetate vanished, and a transparent solution was produced, indicating the successful synthesis of Ag MOD. The as-obtained transparent Ag MOD solution was purified by freeze-drying to remove the water.

Preparation of sintered Ag joints

The Ag MOD was evenly printed on the ENIG Cu substrates in Fig. 1a. According to Fig. 1c, after preheating at 90 °C for 5 min, the Ag MOD was held at 160 °C, 180 °C, and 200 °C for 30 min to create Ag nanostructures. The Ag nanostructures obtained at 160 °C, 180 °C, and 200 °C were named Ag-NS-160, Ag-NS-180, and Ag-NS-200, respectively. The Ag nanostructure of the die was placed directly on the substrate to create a sandwich structure. As no solvent or surface ligands were added, the bonding process was conducted by a simple temperature profile with a rapid ramping rate of 60 °C/min in Fig. 1d, and the holding time and assistant pressure were set to 40 min and 5 MPa, respectively.

Shear test of sintered Ag joints

After fixing samples to the platform of a die-shear tester (STR-1000, Rhesca), the die-shear test was conducted with a shear height of 200 μm and a shear

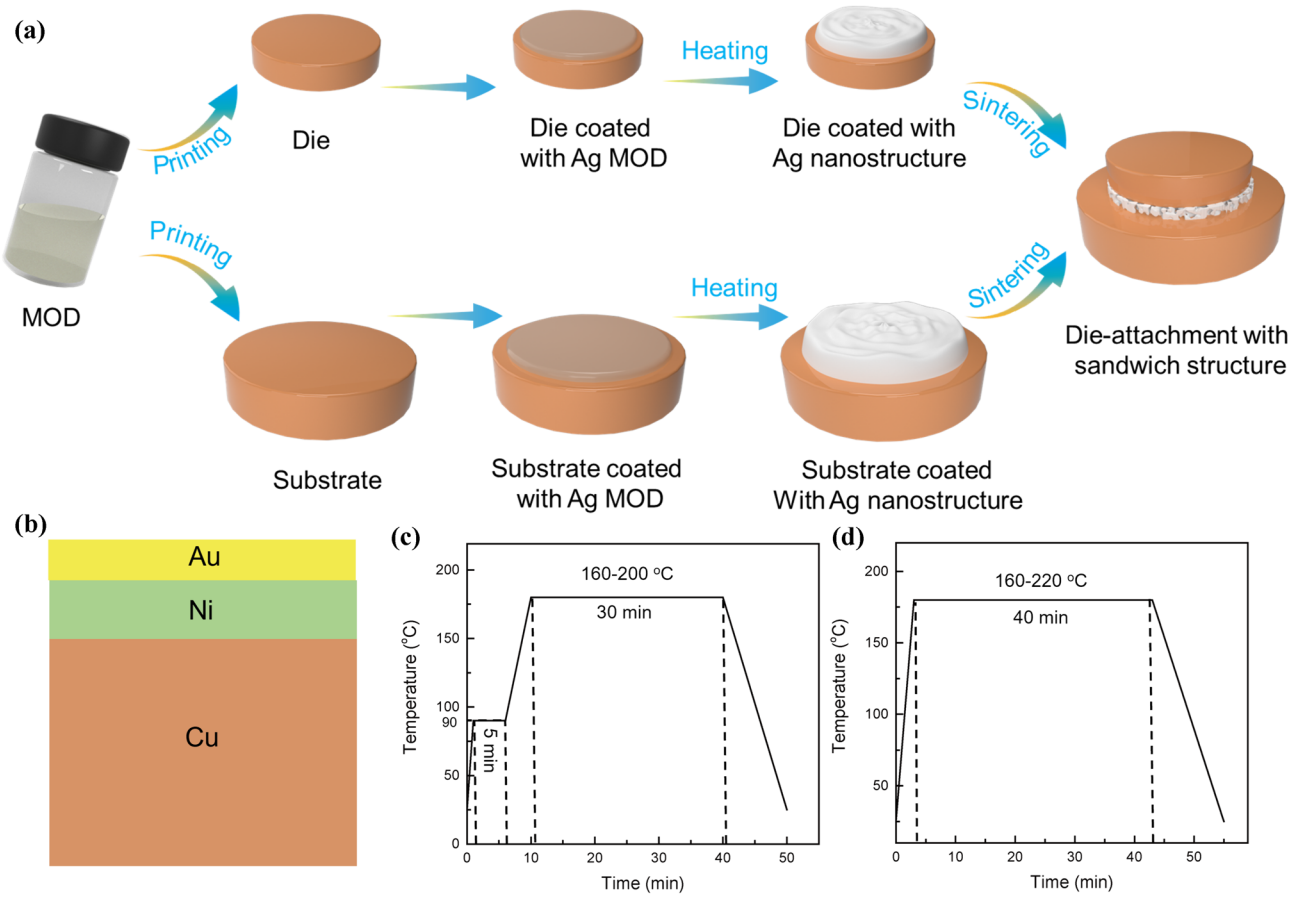

Figure 1 Details of the experiment and heating conditions. Schematic diagrams of the **a** fabrication of sintered Ag joints from the Ag MOD and **b** ENIG Cu substrate. The heating profile of the preparation of the **c** Ag nanostructures and **d** sintered Ag joints.

speed of 1 mm/min in Fig. 2a. Five samples were tested in each group to ensure the reproducibility of experiments.

Characterization

The compositions of the thermally decomposed Ag MODs were investigated using X-ray diffraction (XRD, Ultima IV, Rigaku). The bonding process was performed using a hot-press machine (RB-100D, Asympti Industry Co., Ltd.). The cross section of the sintered Ag joint was fabricated by sandpaper polishing and ion polishing (IB-19530CP, JEOL). SEM (FEI Nova Nana SEM 450) and EDS were used to analyze the microstructure and elemental distribution. TEM (FEI Tecnai G2 F20) was used to investigate the bonding mechanism of the porous Ag nanostructures.

Calculation of particle size

As depicted in Fig. 2b, the diameter of a single Ag particle was measured using the ImageJ software. For each sample, 300 Ag particles were measured to ensure the statistical accuracy of the particle size distribution.

Calculation of porosity and porosity difference

As depicted in Fig. 2c, according to the contrast difference between the Ag phase and pores, the SEM images of the cross sections can be binarized into black and red images using the open-access software, ImageJ. The porosities of the sintered Ag joints are given by the following equation: $P = A_b/A_t$, where A_b is the sum of the black areas and A_t is the total area of the SEM

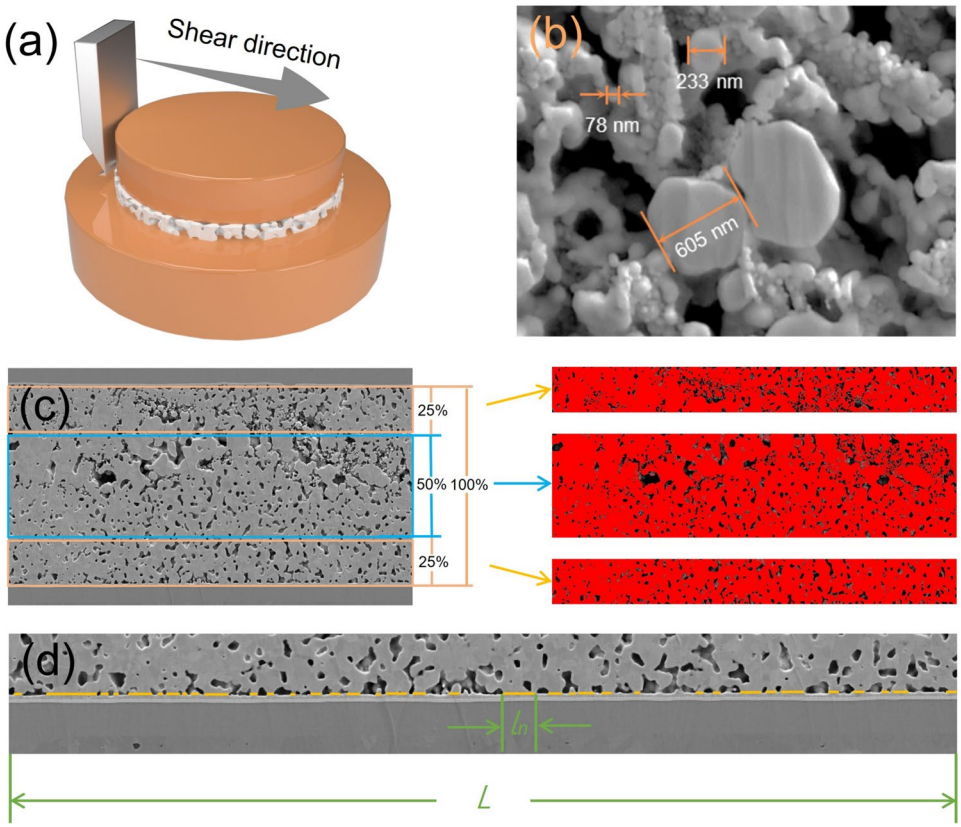

Figure 2 Characterization of samples. **a** schematic diagram of the shear test. Illustrations of the measurement of the **b** size distribution of Ag particles in the Ag nanostructures, **c** porosity of sintered Ag joints, and **d** connection ratio between the sintered Ag joints and substrate based on SEM images.

images. The porosity difference between the edge area and the mid area is given by the following equation: $P_d = |P_e - P_m|$, where P_e and P_m are the porosity of the edge area and mid area, respectively.

Calculation of connection ratio

At the interface shown in Fig. 2d, necks that connect the sintered Ag joint and ENIG Cu substrate are regarded as valid connections, and pores are regarded as invalid connections. Therefore, the connection ratio was calculated by the following equation: $C = \sum l_n / L$, where l_n is the width of the neck and L is the total length of the bonding interface.

Results and discussion

Ag nanostructures derived from the Ag MOD

The thermal decomposition temperature is one of the most crucial factors in determining the thermal decomposition process. The thermal decomposition of the Ag MOD involves the reduction of Ag (*I*), nucleation and crystal growth of Ag, and gasification of organic substances [25, 31–33]. Therefore, the Ag MOD was heated at 160, 180, and 200 °C to investigate the effects of thermal decomposition temperature on the bonding performance of the Ag nanostructures. The top view of the Ag nanostructures is shown in Fig. 3. As depicted in Fig. 3a–c, the three Ag nanostructures were composed of clustered branches. The branches in Fig. 3a_1 consisted of monodispersed Ag NPs and organic intermediate products, whereas those in Fig. 3b_1 and c_1 were comprised of monodispersed Ag NPs and linked Ag NPs, respectively. The corresponding particle sizes in Fig. 3a_2–c_2 increased with increase in thermal decomposition temperature. As shown in Fig. 3f, the *C* content continuously decreased with increase in thermal decomposition temperatures. The results indicated that an increase in temperature not only promoted the thermal decomposition of the Ag MOD, but also resulted in the sintering of Ag NPs. In addition, some Ag NPs smaller than 20 nm, which were barely detected by SEM, were observed by TEM in Fig. 3d, e, and no organic layer was observed on the surface in Fig. 3e. Furthermore, the carbon content of the Ag-NS-180 in Fig. 3f was as low as 0.4%, and

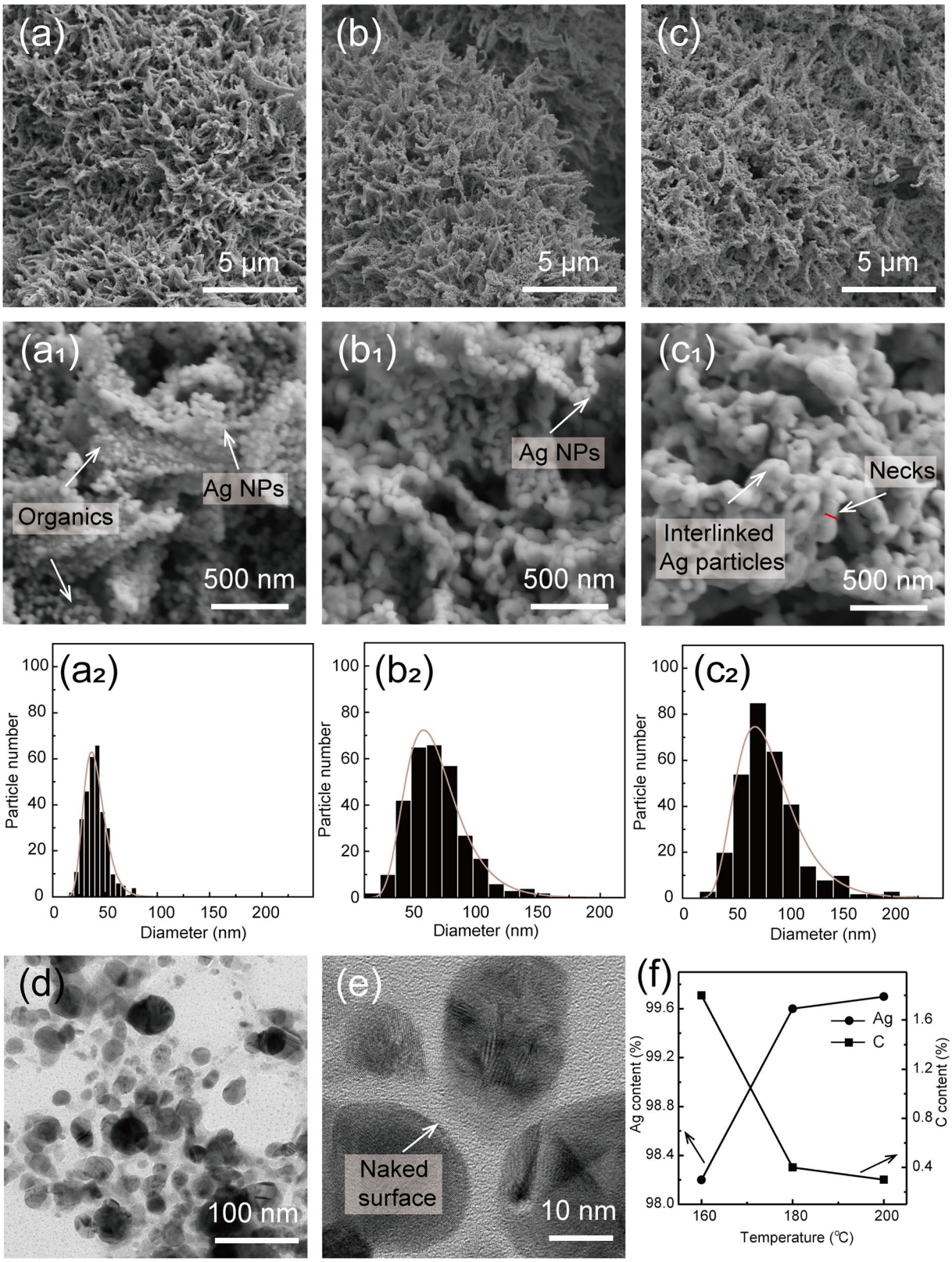
(a)
5 μm
(b)
5 μm
(c)
5 μm
(a1)
Organics
Ag NPs
500 nm
(b1)
Ag NPs
500 nm
(c1)
Necks
Interlinked
Ag particles
500 nm
(a2)
Particle number
Diameter (nm)
(b2)
Particle number
Diameter (nm)
(c2)
Particle number
Diameter (nm)
(d)
100 nm
(e)
Naked
surface
10 nm
(f)
Ag
C
Ag content (%)
C content (%)
Temperature (℃)

◂**Figure 3** Characterization of the Ag nanostructures from the top view. **a** $\mathbf{a_1}$, **b** $\mathbf{b_1}$, and **c** $\mathbf{c_1}$ SEM image of Ag-NS-160, Ag-NS-180, and Ag-NS-200, respectively. $\mathbf{a_2}$–$\mathbf{c_2}$ corresponding particle size distribution. **d** and **e** TEM images of Ag particle of Ag-NS-180. **f** Evolution of Ag and *C* content of Ag nanostructures with thermal decomposition temperature (data from the EDS analysis in Fig. S2 and Fig. S3).

only five Ag characteristic peaks were detected in the XRD pattern of Ag nanostructures in Fig. S1. These results suggest that Ag-NS-180 can be regarded as an organic-free nanomaterial. Therefore, the advantages of the high surface energy of Ag NPs can be exploited without limitations, which is beneficial for enhancing the bonding performance of Ag nanostructures.

Cross sections were observed to reveal the internal information of the Ag nanostructures, as shown in Fig. 4. As shown in Figs. 4a and S4, the porous Ag nanostructure consisted of three distinct layers: I) a NPs layer, II) a loose layer, and III) a dense layer. Magnified SEM images of the three distinct regions in Fig. 4b–b_2, c–c_2, and d–d_2 and the corresponding size distribution in Fig. S5 show that the particle size increased from the NPs layer to the dense layer. The cross sections also demonstrate the effects of the thermal decomposition temperature on the thermal decomposition process. Both spherical Ag NPs and organic intermediate products are shown in Fig. 4b_1. As the thermal decomposition temperature was increased to 180 °C, Ag NPs mixed with monodispersed submicron Ag particles are detected in Fig. 4c_1. When the thermal decomposition temperature was 200 °C, necks between the Ag submicron particles in Fig. 4d_1 indicated that the increased temperatures resulted in the sintering of Ag particles.

Sintered Ag joints derived from the Ag nanostructures

The above results demonstrate that the thermal decomposition temperature significantly affects the thermal decomposition of the Ag MOD and the morphology of the Ag nanostructures. However, the effects of thermal decomposition temperature on bonding performance remain to be investigated to determine the optimal thermal decomposition conditions. Therefore, the Ag nanostructure of the die was directly covered on that of the substrate to form a die-Ag layer-substrate sandwich structure, and this sandwich structure was bonded at a low temperature of 200 °C with 5 MPa for 40 min. As depicted in Fig. 5, Ag-NS-180 exhibited the best bonding performance, resulting in the highest shear strength of 48.6 MPa.

To reveal the evolution of shear strength with thermal decomposition temperature, the fracture surfaces were investigated, as shown in Fig. 6. According to the overall views in Fig. 6a–c, the sintered Ag joints derived from the Ag-NS-160 fractured at the interface region, which followed the fracture model (I) in Fig. S6. The fractures of the sintered Ag joints derived from Ag-NS-180 and Ag-NS-200 agreed with the fracture model (II) shown in Fig. S6, which fractured both at the interface and inside the Ag joints. Therefore, the fracture surfaces of Ag-NS-160 were revealed by two representative regions, Ag joint side and substrate side. Those of Ag-NS-180 and Ag-NS-200 were revealed by three representative regions, inside the Ag joints, Ag joint side, and substrate side. A flat fracture surface with narrow gullies can be observed in Fig. 6a_1. This observation indicated that the joint strength of sintered Ag-NS-180 was governed by the interface condition between sintered Ag and substrate [34]. Monodisperse ductile deformation in Fig. 6a_2, a_3 indicated that connections were formed between the sintered Ag and substrates. However, the bottom regions of gullies were invalid connections, which dramatically decreased the connection area at interface, resulting in poor shear strength in Fig. 5. The formation of gullies may be attributed to the thermal decomposition of the organic intermediate products of Ag-NS-160 in Fig. 4b_1. During this process, rapid gasification of organic substances led to high vapor pressure within the Ag nanostructures, which forced Ag particles to undergo a mandatory displacement [35]. The distance between neighboring Ag particles dramatically increased upon gasification, resulting in huge tunnels inside the Ag joints to facilitate gas release [36, 37]. The negative effects of organics in Ag-NS-160 strongly and directly demonstrated the advantage of organic-free Ag sintering in this study.

For the fracture surfaces derived from Ag-NS-180, continuous ductile deformations with long sliding traces are observed in Fig. 6b_1–b_3. This indicated that significant connections were formed both inside the Ag joint and at the interface. Since the strength of a joint is mainly determined by the internal and interfacial connections [38], these increased connections greatly improved the shear strength to 48.6 MPa in Fig. 5. When the thermal decomposition temperature was 200 °C, monodispersed ductile deformations in

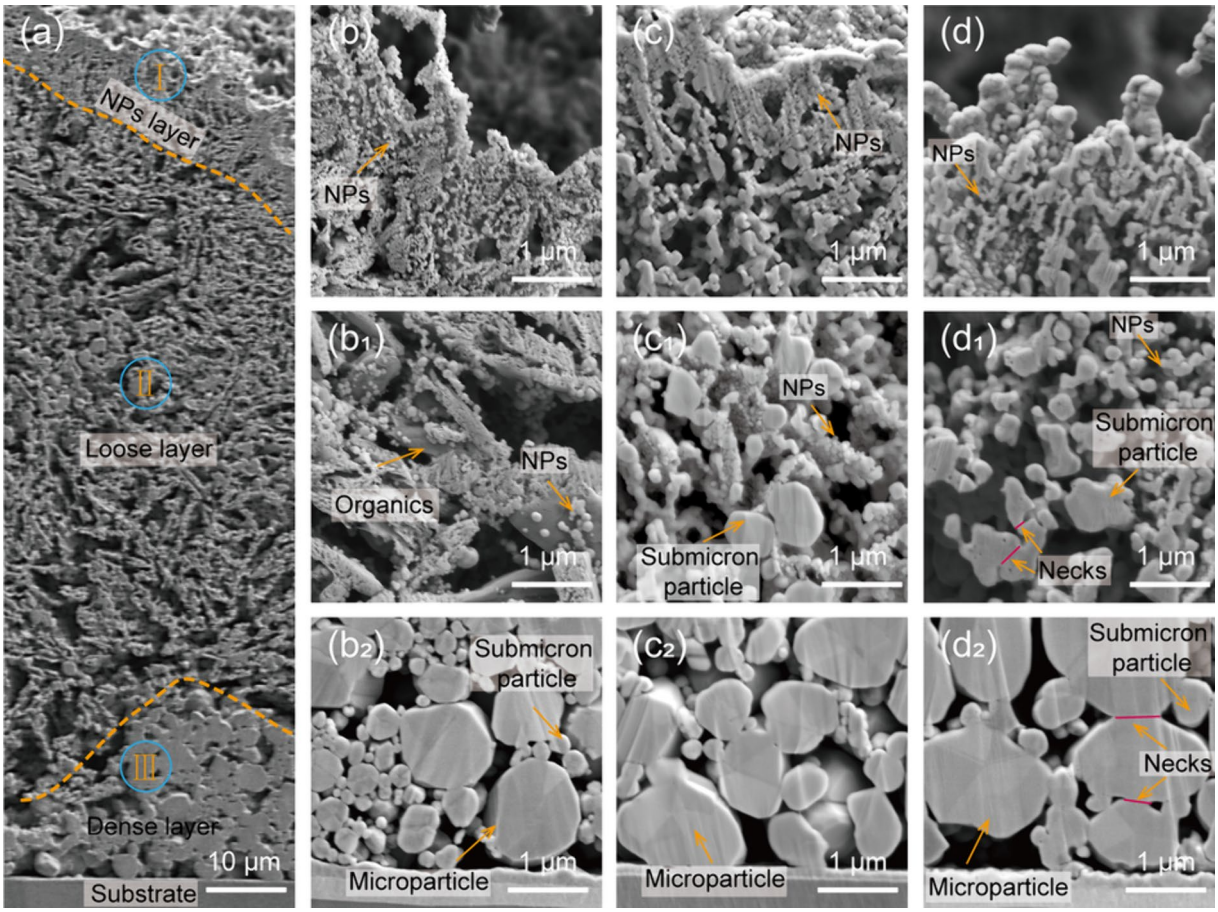

Figure 4 Characterizations of the Ag nanostructures from the cross-sectional view. **a** overall view of Ag-NS-180. High-magnification views of region **b** I, $\mathbf{b_1}$ II, and $\mathbf{b_2}$ III of Ag-NS-160. High-magnification views of region **c** I, $\mathbf{c_1}$ II, and $\mathbf{c_2}$ III of Ag-NS-180. High-magnification views of region **d** I, $\mathbf{d_1}$ II, and $\mathbf{d_2}$ III of Ag-NS-200.

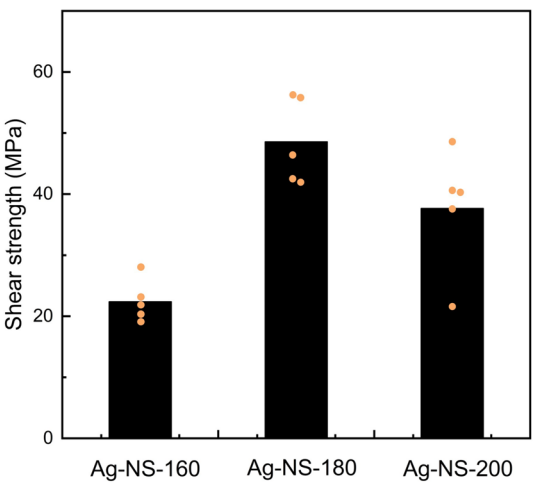

Figure 5 Shear strength of the Ag joints sintered at 200 °C with 5 MPa for 40 min.

Fig. 6c_1–c_3 indicated insufficient sintering of Ag-NS-200. According to sintering theory, sintering occurs by reducing Gibbs free energy, which involves substituting high-energy surfaces with low-energy grain boundaries [39, 40]. As shown in Fig. 4, the pre-sintering of Ag particles in Ag-NS-200 led to an increase in particles size. Larger particles demonstrate a smaller specific surface area and thus lower surface energy [39]. Consequently, the reduction in surface energy led to a decrease in shear strength with increase in decomposition temperature.

The fracture surfaces in Fig. 6 show that the thermal decomposition temperature significantly affected the bonding performance of the Ag nanostructures. To further validate this effect, sintered Ag joints were observed through cross-sectional analysis, as shown in Fig. 7. The bondline thickness (thickness of sintered Ag layer) in Fig. 7a was notably thinner than those

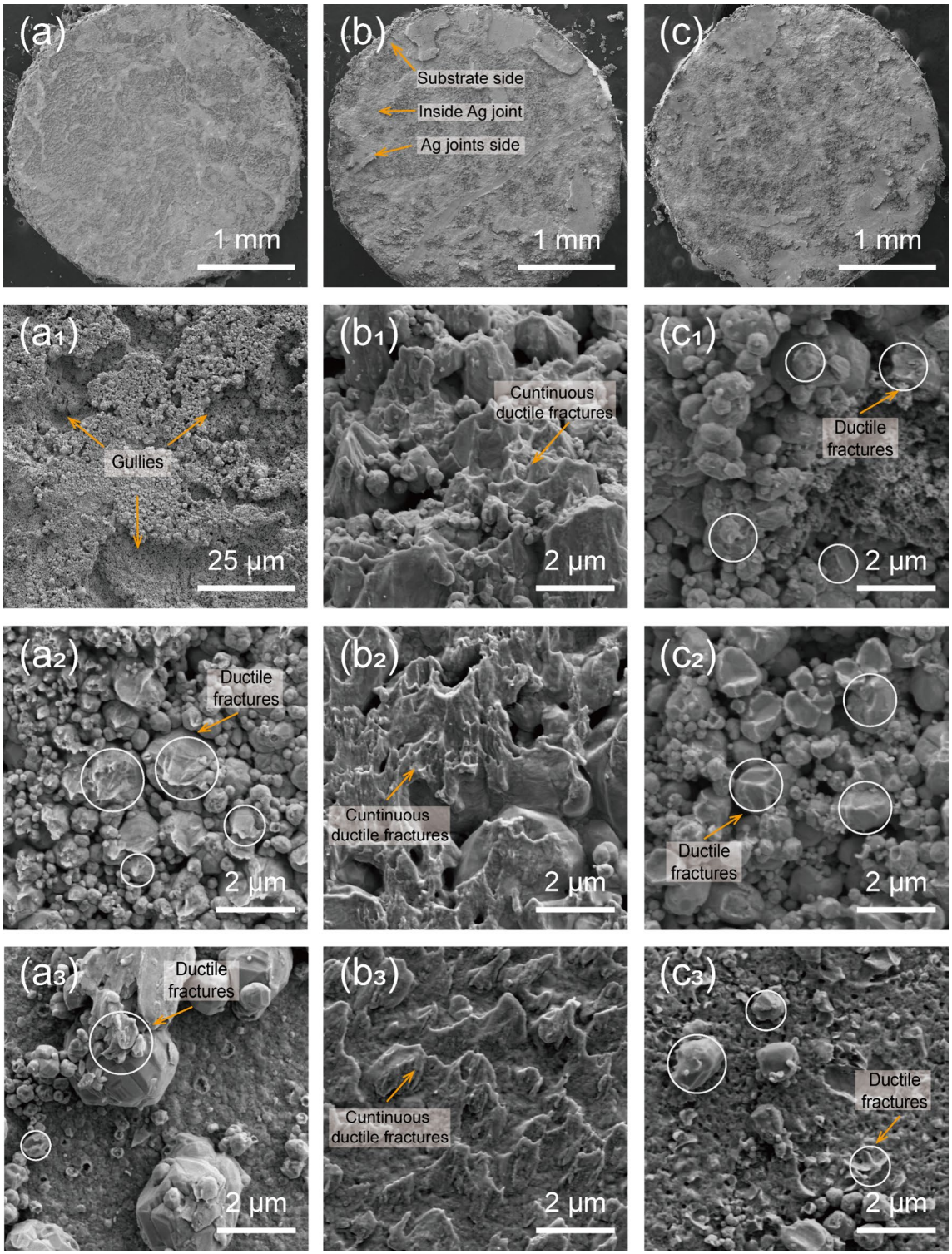

Figure 6 Microstructure of the fracture surfaces of Ag joints sintered at 200 °C. SEM images of the fracture surface of the sintered Ag joint derived from **a**–**a**$_3$ Ag-NS-160, **b**–**b**$_3$ Ag-NS-180, and **c**–**c**$_3$ Ag-NS-200. **b**$_1$ **c**$_1$ Inside the Ag joint, **a**$_1$ **a**$_2$ **b**$_2$ **c**$_2$ Ag joint side, and **a**$_3$ **b**$_3$ **c**$_3$ substrate side.

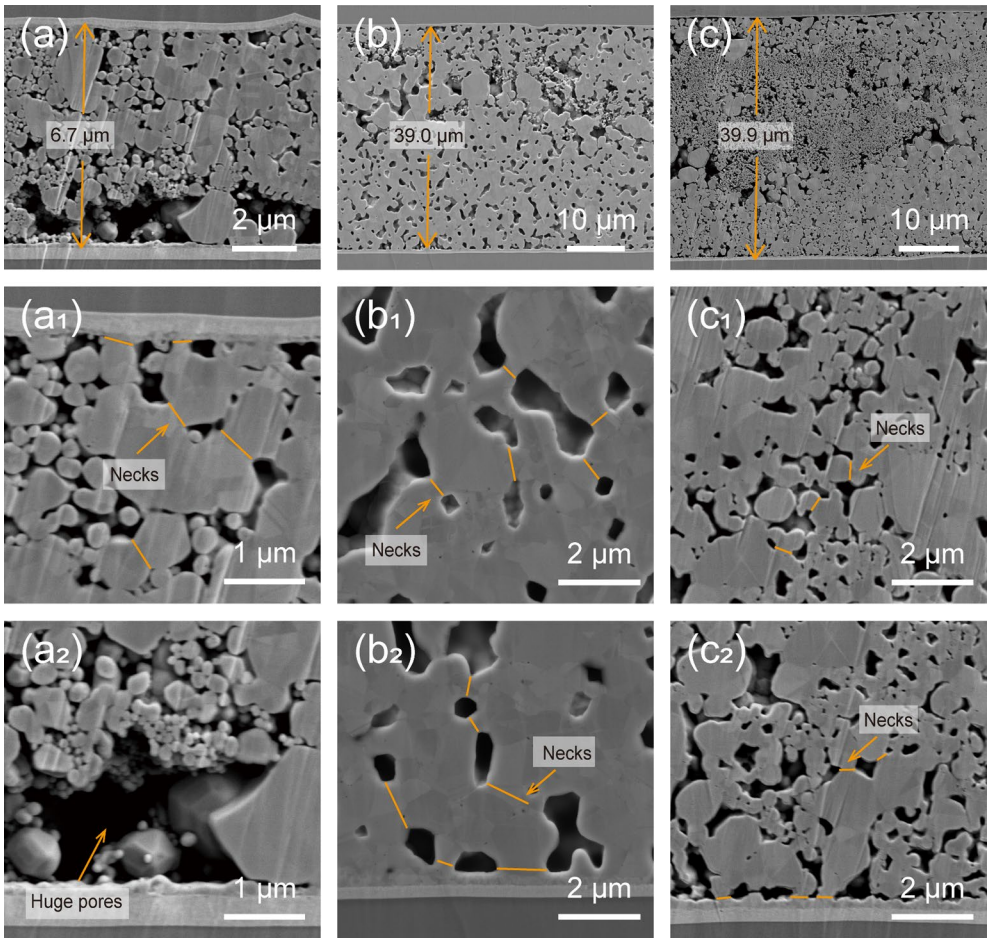

Figure 7 Microstructure of the cross sections of Ag joints sintered at 200 °C. SEM images of the cross sections of the sintered Ag joint derived from **a**–$\mathbf{a_2}$ Ag-NS-160, **b**–$\mathbf{b_2}$ Ag-NS-180, and **c**–$\mathbf{c_2}$ Ag-NS-200. $\mathbf{b_1}$ $\mathbf{c_1}$ Inside the Ag joint and $\mathbf{b_2}$ $\mathbf{c_2}$ interface region.

in Fig. 7b, c. This can be attributed to the presence of organic intermediate products, which imparted fluidity to Ag-NS-160. During the bonding process, some Ag-NS-160 particles were squeezed out, leading to a reduction in thickness. Although necks formed both inside the sintered Ag joint and at the interface region in Fig. 7a_1, the large pores in Fig. 7a, a_2 dramatically deteriorated the connection between the sintered Ag joints and the substrates, resulting in a lower shear strength in Fig. 5. Additionally, the prominent pores illustrated in Fig. 7a, a_2 induced by the gasification of organic compounds corresponded to the gullies in Fig. 6a_1 [36, 37]. This is because fracture of the Ag joints occurred at interface in Fig. 6a_1, and the huge pores in Fig. 7a, a_2 were distributed at the interface regions. In summary, this observation further proves the seriously negative effects of trapped organics in the Ag nanostructures.

The necks in Fig. 7b_1, b_2 were thicker than those in Fig. 7c_1, c_2, indicating that the bonding performance of Ag-NS-180 was better than that of Ag-NS-200. The observed phenomenon can be attributed to the smaller particle size of Ag-NS-180 compared to Ag-NS-200, resulting in a higher surface energy for Ag-NS-180 [39]. With a high surface energy, Ag-NS-180 was sintered into robust Ag joints with the highest shear strength in Fig. 5. As shown in Fig. 8, the thermal decomposition temperature can affect the bonding performance of Ag nanostructures based on two factors: the content of the organic intermediate products and the sintering of the Ag particles. Residual organic intermediate products in Ag-NS-160 can cause large pores in sintered Ag joints during the bonding process. However, the pre-sintering of Ag particles in Ag-NS-200 increased the particle size and reduced the surface energy, bonding performance, and shear strength. Therefore, the thermal decomposition temperature should be carefully determined to ensure that severe Ag particle sintering does not occur while the Ag MOD is sufficiently decomposed.

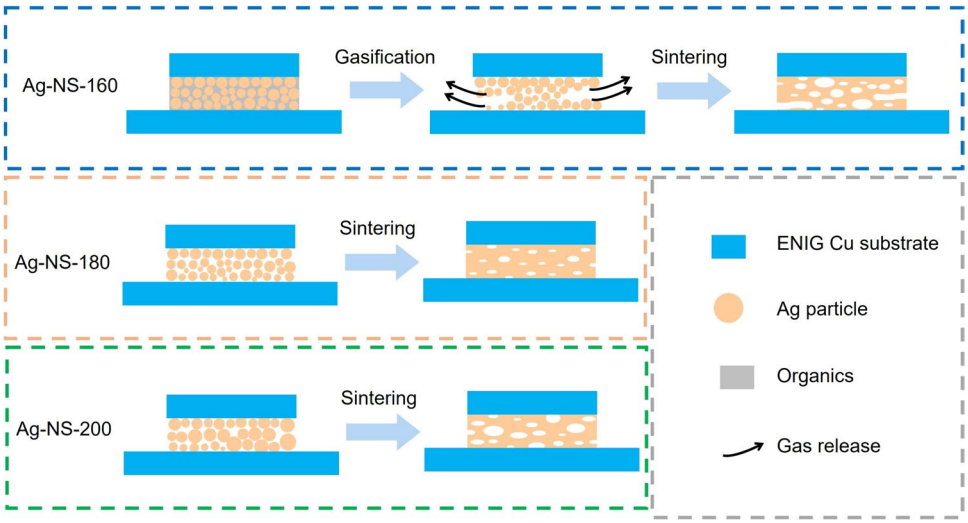

Figure 8 Schematic diagram illustrating the sintering process of Ag nanostructures.

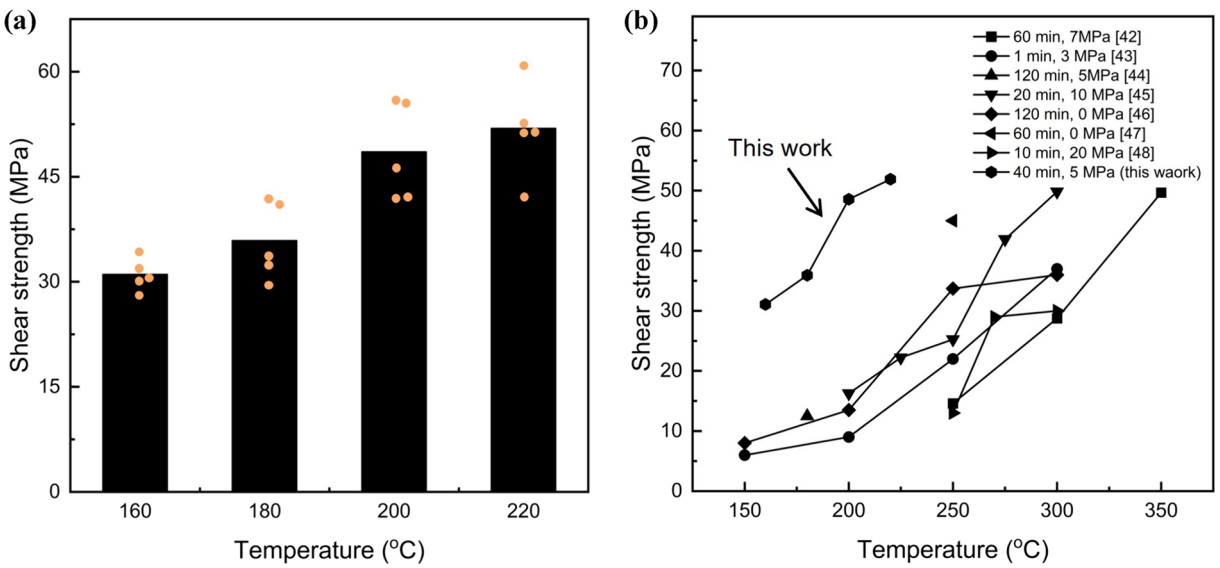

Figure 9 Shear strength of sintered Ag joints derived from Ag-NS-180 at different temperatures. **a** Shear strength of sintered Ag joints using Ag nanostructures with different bonding temperatures. **b** Comparison of shear strength between sintering Ag nanostructures derived from the MOD and sintering Ag particle pastes.

Low-temperature bonding performance of Ag-NS-180

The above results indicate that Ag-NS-180 exhibited the best bonding performance, resulting in the highest shear strength of 48.6 MPa. To further understand the bonding performance of Ag-NS-180, it was bonded in a temperature range of 160–220 °C, and the evolution of shear strength with bonding temperature is shown in Fig. 9. The shear strength increased with increase in bonding temperatures, and a high shear strength of 51.9 MPa was achieved at 220 °C. To demonstrate the advantage of low-temperature bonding, a comparison of the shear strengths between Ag porous nanostructure bonding and Ag paste sintering is shown in Fig. 9b [41–47]. It can be seen that Ag nanostructures showed the best bonding performance in the temperature range 160–200 °C, and the shear strength 48.6 MPa of Ag porous nanostructures at 200 °C was approximately three times that of sintered Ag paste in previous reports [44]. Especially, for a low temperature of

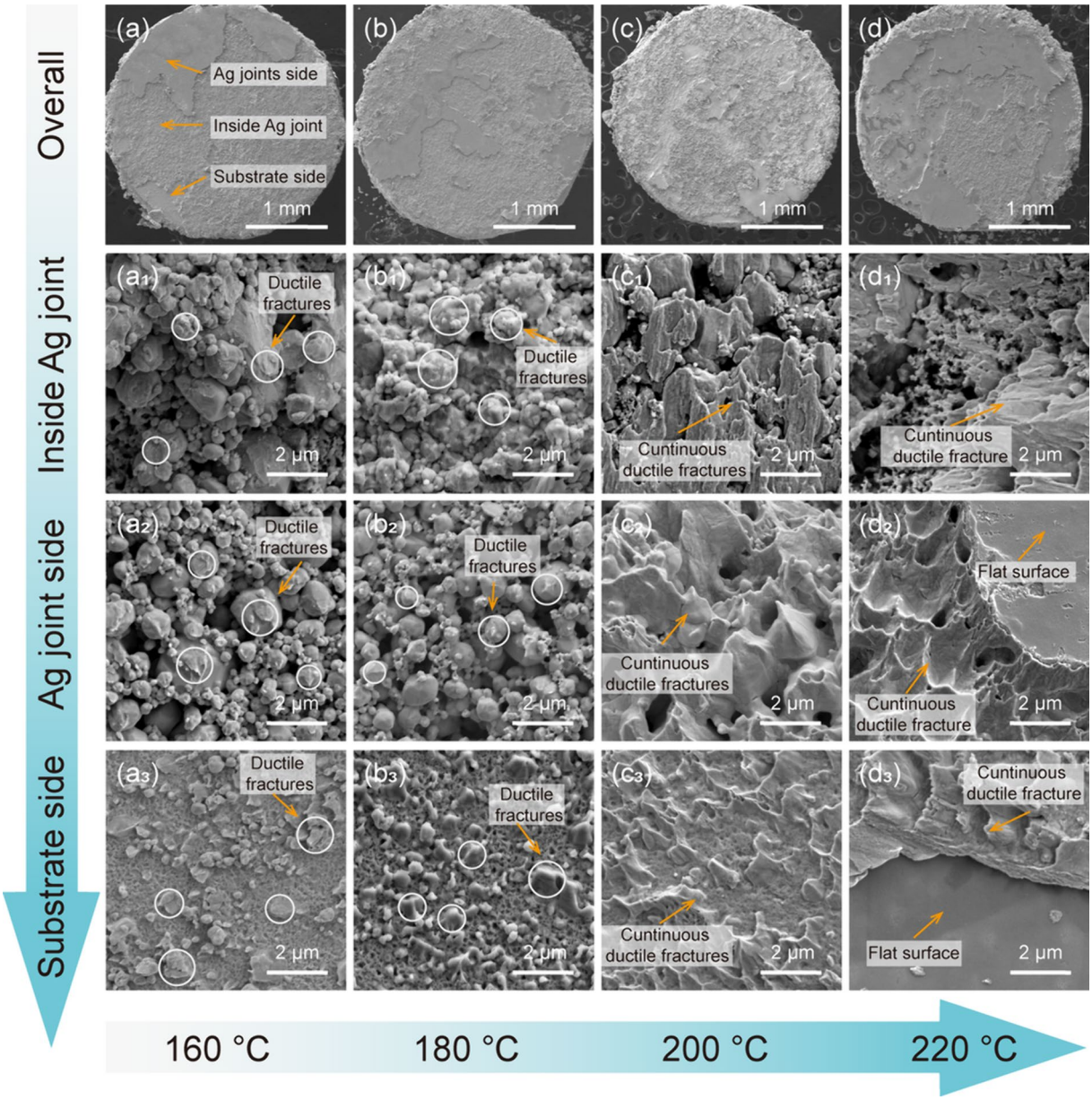

Figure 10 Characterization of the fracture surfaces with different bonding temperatures. SEM images of the fracture surface of the sintered Ag joints derived from Ag-NS-180 at **a**–**a**$_3$ 160 °C, **b**–**b**$_3$ 180 °C, **c**–**c**$_3$ 200 °C, and **d**–**d**$_3$ 220 °C.

160 °C, Ag pastes hardly formed a sintered Ag joint with a shear strength over 10 MPa, because 160 °C is even lower than the boiling point of most used organics in the Ag pastes such as 288 °C of triethylene glycol [42], 217 °C of terpineol [42], and 340 °C of polyvinyl pyrrolidone (PVP) [44]. By contrast, a remarkable shear strength of 31.1 MPa was achieved by Ag porous nanostructures at 160 °C. These excellent joint properties indicated the superior low-temperature bonding properties of Ag-NS-180.

The Ag-NS-180 showed a remarkable bonding performance in a low-temperature range of 160–220 °C, and the shear strength increased with increase in temperature. The fracture surfaces revealed the shear strength evolution with temperature mechanism. As depicted in Fig. 10a–d, their fracture model was in line with the model (II) Fig. S6. Therefore, the microstructures of the fracture surfaces were characterized in the same way as shown in Fig. 6b, c. When the bonding temperatures were 160 °C and 180 °C, monodispersed

ductile fractures are detected in Fig. 10$a_{1–2}$, $b_{1–2}$, indicating sintering of Ag particles occurred inside the sintered Ag joint and at the interface. As the temperature was over 200 °C, continuous ductile deformations with long sliding traces are observed in Fig. 10$c_{1–2}$, $d_{1–2}$. This indicates significantly enhanced sintering of the Ag particles inside the sintered Ag joint and at the interface. In terms of the substrate side in Fig. 10a_3–d_3, monodispersed and small ductile fractures were converted to interconnected ductile fractures with long sliding traces, implying that the interconnection between the sintered Ag joints and substrates became stronger from 160 to 220 °C. The results showed that increasing the bonding temperature promoted the sintering of the Ag nanostructures and resulted in an increase in the shear strength, as shown in Fig. 9a. This tendency of shear strength with temperature had also been confirmed in previous studies but in higher temperature ranges (Fig. 9b) [41–47].

In addition, the ductile deformations and flat fracture surfaces are observed in Fig. 10d_2, d_3. To figure out the flat fracture surfaces, the fracture surfaces of the Ag joint side and substrate side were characterized by EDS. Visible Au in Fig. 11a_3 and Ni in Fig. 11b_5 were

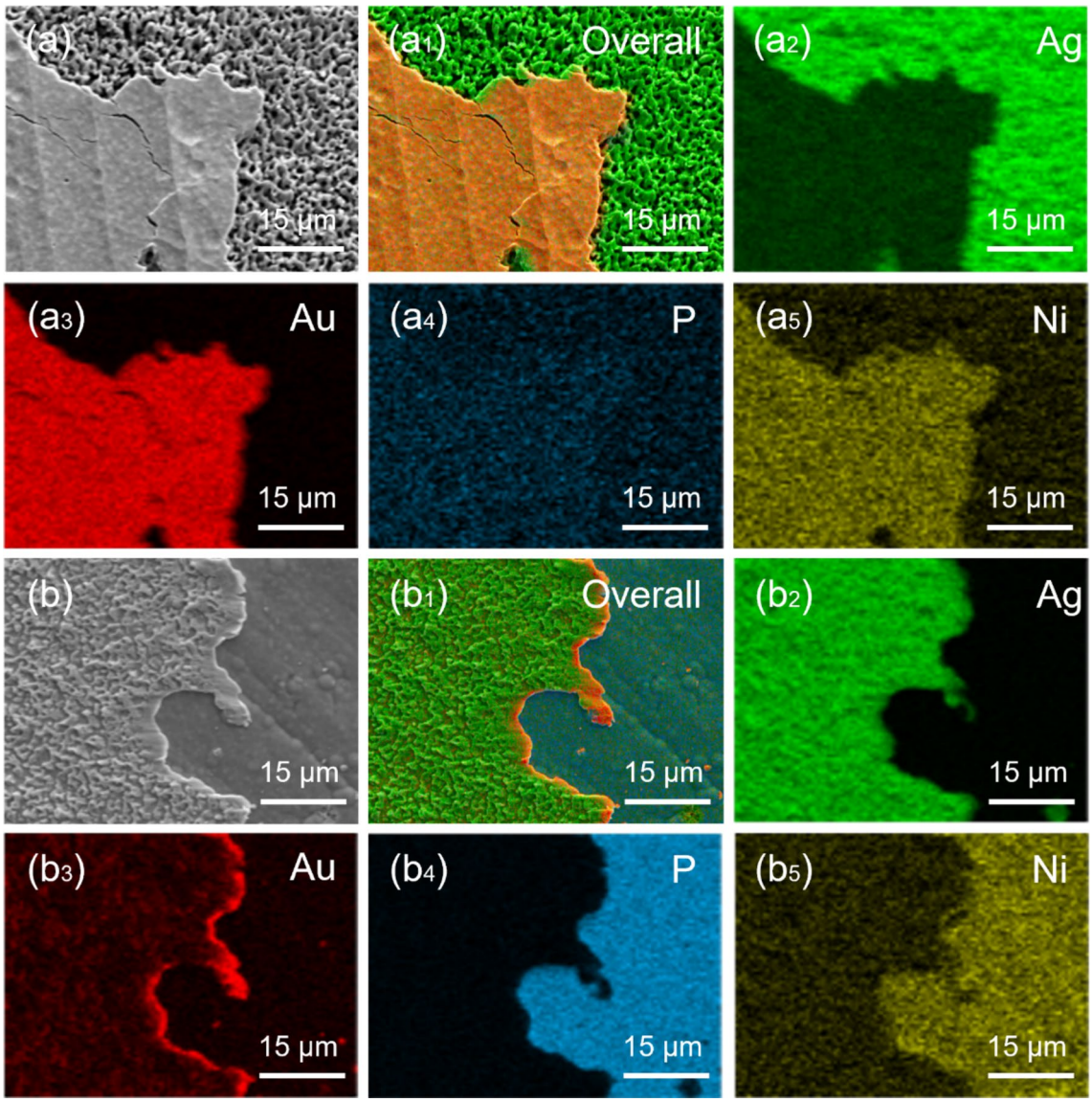

Figure 11 Element distribution of the fractures surface of sintered Ag joints derived from Ag-NS-180 at 220 °C with 5 MPa for 40 min. EDS mapping at **a**–**a_5** the Ag joints side and **b**–**b_5** substrate side.

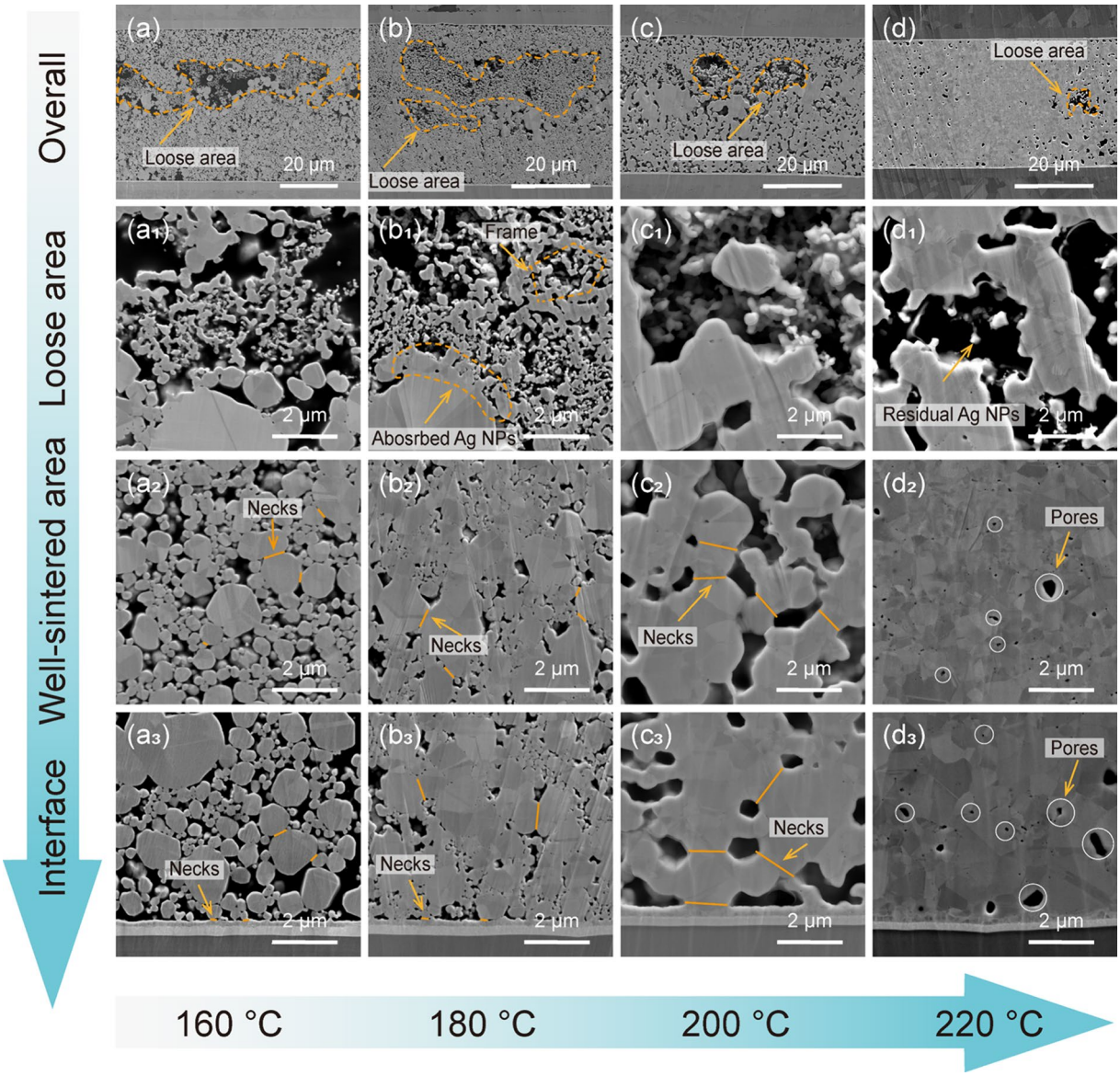

Figure 12 Characterization of the cross sections with different bonding temperatures. SEM images of the fracture surface of the sintered Ag joint derived from Ag-NS-180 at **a**–**a**$_3$ 160 °C, **b**–**b**$_3$ 180 °C, **c**–**c**$_3$ 200 °C, and **d**–**d**$_3$ 220 °C.

detected at the flat fracture surface of Ag joint side and substrate side, respectively. This means the flat fracture surfaces in Fig. 10d$_2$, d$_3$ are Ag layer and Ni layer, respectively. The appearance of Au layer on the Ag joints side indicates that the Au layer was stripped off the Ni layer during the die-shear test. This observation also proved that the elevated temperature promoted the connection between the sintered Ag and the substrate, which was consistent with the conclusions of Fig. 10.

The cross sections obtained from 160 to 220 °C are observed and listed in Fig. 12. As shown in Fig. 12a–d, the Ag joints were composed of two distinct areas: (I) a well-sintered area and (II) a loose area. The well-sintered area was close to the interface between the sintered Ag and the substrate, and the loose area was at the center of the sintered Ag joints. In addition, the loose area can be considered a defect area in the sintered Ag joint because a larger number of isolated Ag NPs were observed in the high-magnification view in Fig. 12a1–d1. Therefore, three types of porosities were calculated according to their positions in the cross section, and the porosity information is shown in Fig. 13a, b.

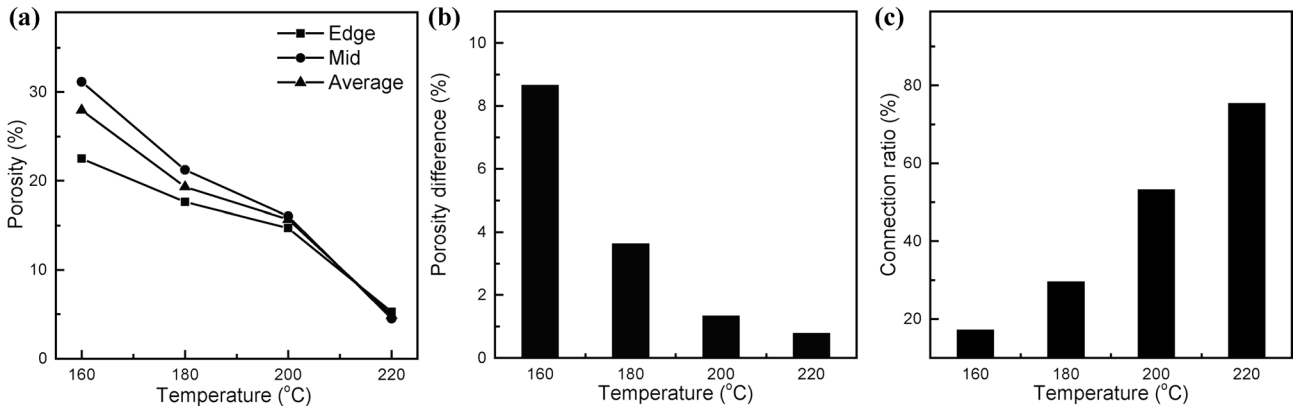

Figure 13 Joint information derived from cross sections of sintered Ag joints derived from Ag-NS-180. Evolution of **a** porosity, **b** porosity difference between the edge and mid area, and **c** connection ratio with the bonding temperature.

As the temperature increased from 160 to 220 °C, there was a noticeable reduction in the loose area in Fig. 12a–d, resulting in a decrease in the porosity in Fig. 13a. As shown in Fig. 12a_1–d_1, the reduction in the loose area can be attributed to the gradual absorption of Ag NPs in the loose area by the well-sintered area. As the looser area was converted into a well-sintered area, the porosity difference between the edge and middle areas decreased, as shown in Fig. 13b. In addition, necks between large particles were evident, indicating that interconnections inside the sintered Ag joint were initially established in Fig. 12a_2. Like the skeleton in the human body, these well-connected particles provide support for the sintered Ag joints, resulting in remarkable shear strength of 31.1 MPa at a low temperature of 160 °C. This means appropriate temperatures play an important role in triggering the sintering of Ag nanoparticles [48] As the bonding temperature increased to 200 °C, the sintered Ag joints were converted into a continuous porous structure with thick necks in Fig. 12c_2. After densification, a dense Ag joint with isolated round pores was obtained at 220 °C in Fig. 12d_2, and the corresponding shear strength reached the maximum value of 51.9 MPa. These morphology changes were attributed to the elevated sintering temperature promoted the mass transport mechanisms, such as surface diffusion and volume diffusion, responsible for sintering [49, 50].

In terms of the interface area, shown in Fig. 12a_3–d_3, similar morphological changes were observed on the Ag joint side, and no apparent changes were detected in the metallization layer of the ENIG Cu substrates. However, the necks between the sintered Ag joints and substrates became thicker with increase in temperature, which enhanced the connection ratio, as shown in Fig. 13c, and thus improved the shear strength. In summary, increasing the temperature resulted in an increase in the shear strength by reducing the loose area, converting the Ag nanostructure into dense sintered Ag joints, and promoting connections with the substrates.

Mechanism of high shear strength

To further reveal the reason for the excellent joint properties, the sintered Ag joint derived from Ag-NS-180 at 200 °C was observed by TEM, as shown in Fig. 14. As shown in Fig. 14a, massive grain boundaries were visible and randomly distributed in the sintered Ag joints. As previously reported, the fractures of bulk metals tend to propagate along the direction of the grain boundaries [51]. Therefore, these randomly distributed grain boundaries can prevent the spread of fractures, making it difficult for the fractures to propagate in a single direction, resulting in excellent joint properties. In the interface region shown in Fig. 14b, a distinct layer above the Au layer was observed, which can also be seen in Fig. 4b_2–d_2. This implies that this distinct layer was already generated during the thermal decomposition of the Ag MOD. Based on the EDS line scan results shown in Fig. 14c, this line could be attributed to the Ag–Au mixing layer. No pores were detected at the interface between the Au layer and the mixing layer in Fig. 14b, indicating an excellent connection between them. The grain size in the Ag–Au layer was much smaller than that inside

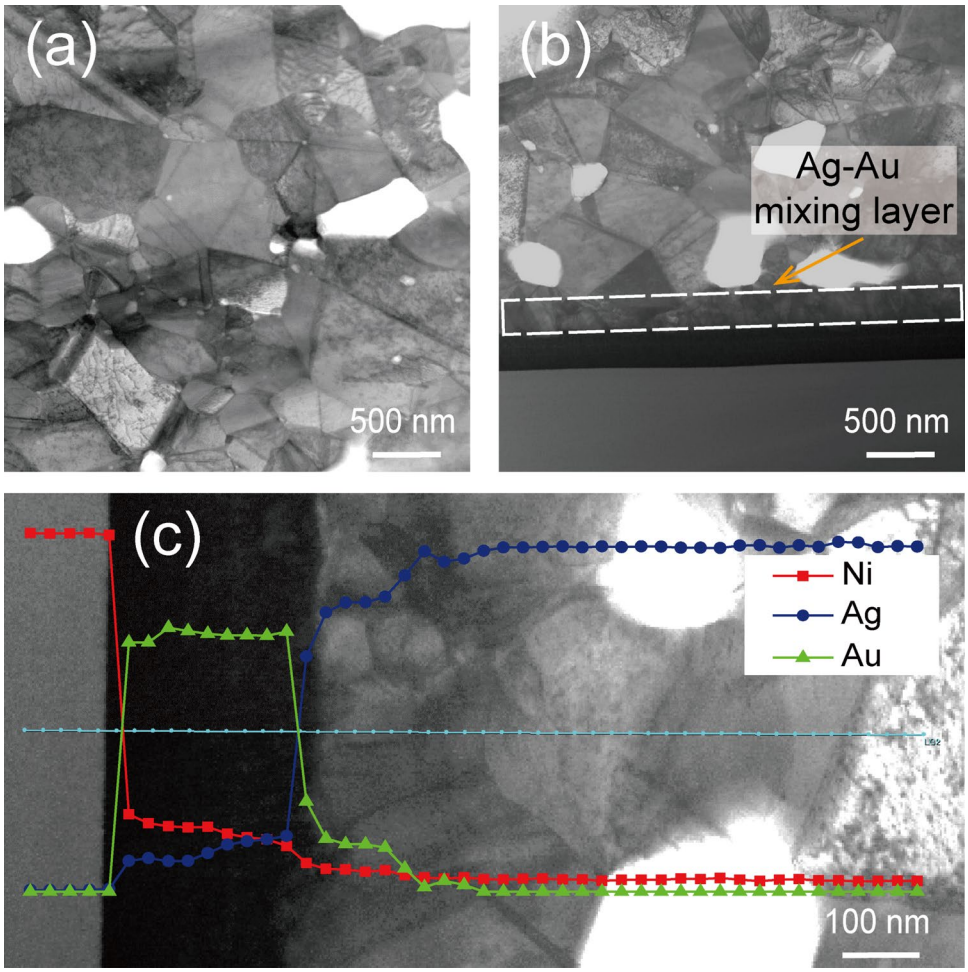

Figure 14 TEM characterization of sintered Ag joints derived from Ag-NS-180 at 200 °C with 5 MPa for 40 min. TEM images of **a** the sintered Ag joints and **b** the interface between the sintered Ag joint and substrate. **c** EDS line scan at the interface region.

the sintered Ag joint. Consequently, the connection between sintered Ag joints and substrate was significantly improved by the existence of the Ag–Au mixing layer, and this connection was even better than the connection between the Au layer and Ni layer when the bonding temperature was 220 °C. In summary, the randomly distributed grain boundaries and automatically generated Ag–Au mixing layer contributed to the excellent joint properties at low temperatures.

Conclusion

In this study, the effects of the thermal decomposition temperature of the Ag MOD on the bonding performance of Ag nanostructures were investigated. The results showed that the thermal decomposition temperature could determine two factors of the Ag nanostructures: I) the content of organic intermediate products and II) the sintering of Ag particles. At a low thermal decomposition temperature of 160 °C, the existence of organic intermediate products resulted in gaseous products. The removal of gaseous products led to large pores inside the sintered Ag joints, which deteriorated the joint properties. Although the Ag MOD thoroughly decomposed at 200 °C, sintering between the Ag particles of the Ag nanostructures decreased the surface energy and driving force for sintering. Comparatively, tiny Ag NPs with naked surfaces rendered remarkable bonding performance to Ag-NS-180, resulting in a shear strength of 48.6 MPa at 200 °C. The bonding performance of the Ag-NS-180 was further investigated by bonding in a temperature range of 160–220 °C. The shear strength (31.1 MPa obtained at 160 °C indicates that Ag-NS-180 possesses an excellent low-temperature bonding performance. In summary, Ag MOD thermal decomposition temperature-dependent bonding performance of the Ag MOD, explored herein, provides a new understanding for optimizing Ag nanostructure sintering.

Acknowledgements

This study was financially supported by the China Scholarship Council [grant number: 202106340038].

Author contributions

Chuncheng Wang contributed to investigation, data analysis, and wrote the original draft. Hiroaki Tatsumi contributed to revision, editing, and supervision. Hiroshi Nishikawa helped in conceptualization, data analysis, revision, editing, supervision, and project administration.

Funding

Open Access funding provided by Osaka University. China Sponsorship Council, 202106340038, Chuncheng Wang.

Declarations

Conflict of interest The authors declare that they have no known competing financial interests or personal relationships that could have appeared to influence the work reported in this paper.

Supplementary Information The online version contains supplementary material available at https://doi.org/10.1007/s10853-024-10250-1.

References

[1] Dudina DV, Bokhonov BB, Olevsky EA (2019) Fabrication of porous materials by spark plasma sintering: a review. Materials. https://doi.org/10.3390/ma12030541

[2] Hassan ZK (2019) Production of metal foams by using powder metallurgy method. AIP Conf Proc 2123:020004. https://doi.org/10.1063/1.5116931

[3] Tang H, Peng Z, Gu F et al (2021) Chromium-promoted preparation of forsterite refractory materials from ferronickel slag by microwave sintering. Ceram Int 47:10809–10818. https://doi.org/10.1016/j.ceramint.2020.12.198

[4] Ji H, Zhou J, Liang M et al (2018) Ultra-low temperature sintering of Cu@Ag core-shell nanoparticle paste by ultrasonic in air for high-temperature power device packaging. Ultrason Sonochem 41:375–381. https://doi.org/10.1016/j.ultsonch.2017.10.003

[5] Botter N, Khazaka R, Avenas Y et al (2022) Power module using ceramic heat sink and multilayers silver sintering. IEEE Trans Compon Packaging Manuf Technol 12:1082–1090. https://doi.org/10.1109/TCPMT.2022.3179432

[6] Park B, Saito M, Mizuno J, Nishikawa H (2022) Robust shear strength of Cu–Au joint on Au surface-finished Cu disks by solid-state nanoporous Cu bonding. Microelectron Eng 260:111807. https://doi.org/10.1016/j.mee.2022.111807

[7] Xie Y, Wang Y, Mei Y et al (2018) Rapid sintering of nano-Ag paste at low current to bond large area (> 100 mm^2) power chips for electronics packaging. J Mater Process Technol 255:644–649. https://doi.org/10.1016/j.jmatprotec.2018.01.017

[8] Shen Y-A (2024) Effect of indium addition on mechanical, thermal, and soldering properties of eutectic Sn–9Zn alloy. Mater Chem Phys 315:128992. https://doi.org/10.1016/j.matchemphys.2024.128992

[9] Wu L, Qian J, Yu J et al (2021) Optimal Cu paste thickness for large-area Cu-Cu joint. Mater Lett 291:129533. https://doi.org/10.1016/j.matlet.2021.129533

[10] Gao R, He S, Li J et al (2020) Interfacial transformation of preoxidized Cu microparticles in a formic-acid

atmosphere for pressureless Cu–Cu bonding. J Mater Sci: Mater Electron 31:14635–14644. https://doi.org/10.1007/s10854-020-04026-x

[11] Kino H, Hashiguchi H, Tanikawa S et al (2016) Effect of local stress induced by thermal expansion of underfill in three-dimensional stacked IC. Jpn J Appl Phys 55:04EC03. https://doi.org/10.7567/JJAP.55.04EC03

[12] Lei TG, Calata JN, Lu G-Q et al (2010) Low-temperature sintering of nanoscale silver paste for attaching large-area (100 mm^2) chips. IEEE Trans Compon Packag Technol 33:98–104. https://doi.org/10.1109/TCAPT.2009.2021256

[13] Dillon SJ, Ma Y, Oyang J et al (2023) Interface nucleation rate limited densification during sintering. Acta Mater 242:118448. https://doi.org/10.1016/j.actamat.2022.118448

[14] Moon K-S, Dong H, Maric R et al (2005) Thermal behavior of silver nanoparticles for low-temperature interconnect applications. J Electron Mater 34:168–175. https://doi.org/10.1007/s11664-005-0229-8

[15] Joo S, Baldwin DF (2010) Adhesion mechanisms of nanoparticle silver to substrate materials: identification. Nanotechnology 21:055204. https://doi.org/10.1088/0957-4484/21/5/055204

[16] Siow KS (2012) Mechanical properties of nano-silver joints as die attach materials. J Alloys Compd 514:6–19. https://doi.org/10.1016/j.jallcom.2011.10.092

[17] Jiu J, Zhang H, Nagao S et al (2016) Die-attaching silver paste based on a novel solvent for high-power semiconductor devices. J Mater Sci 51:3422–3430. https://doi.org/10.1007/s10853-015-9659-8

[18] Wang W, Zou G, Jia Q et al (2020) Mechanical properties and microstructure of low temperature sintered joints using organic-free silver nanostructured film for die attachment of SiC power electronics. Mater Sci Eng: A 793:139894. https://doi.org/10.1016/j.msea.2020.139894

[19] Suganuma K, Sakamoto S, Kagami N et al (2012) Low-temperature low-pressure die attach with hybrid silver particle paste. Microelectron Reliab 52:375–380. https://doi.org/10.1016/j.microrel.2011.07.088

[20] Roh M-H, Nishikawa H, Tsutsumi S et al (2016) Pressureless bonding by micro-sized silver particle paste for high-temperature electronic packaging. Mater Trans 57:1209–1214. https://doi.org/10.2320/matertrans.MD201513

[21] Lee Y-J, Lee J-H (2023) Ultrafast sinter bonding between Cu finishes under moderate compression using in situ derived Ag Formed via Low-temperature decomposition of Ag_2O in the bonding paste. Met Mater Int 29:1775–1785. https://doi.org/10.1007/s12540-022-01320-7

[22] Kim K-S, Myung W-R, Jung S-B (2012) Effects of sintering conditions on microstructure and characteristics of screen-printed Ag thin film. Electron Mater Lett 8:309–314. https://doi.org/10.1007/s13391-012-1102-6

[23] Kim D, Chen C, Nagao S, Suganuma K (2020) Mechanical characteristics and fracture behavior of GaN/DBA die-attached during thermal aging: pressure-less hybrid Ag sinter joint and Pb–5Sn solder joint. J Mater Sci: Mater Electron 31:587–598. https://doi.org/10.1007/s10854-019-02563-8

[24] Wang C, Tatsumi H, Xu L et al (2024) Transparent liquid Ag-based complex for the facile preparation of robust sintered Ag joints in power devices. ACS Appl Electron Mater. https://doi.org/10.1021/acsaelm.3c01629

[25] Yang W, Liu C, Zhang Z et al (2012) One step synthesis of uniform organic silver ink drawing directly on paper substrates. J Mater Chem 22:23012–23016. https://doi.org/10.1039/C2JM34264B

[26] Vaseem M, McKerricher G, Shamim A (2016) Robust design of a particle-free silver-organo-complex ink with high conductivity and inkjet stability for flexible electronics. ACS Appl Mater Interfaces 8:177–186. https://doi.org/10.1021/acsami.5b08125

[27] Zheng S, Sun Y, Xue H et al (2022) Dual-ligand and hard-soft-acid-base strategies to optimize metal-organic framework nanocrystals for stable electrochemical cycling performance. Natl Sci Rev 9:nwab197. https://doi.org/10.1093/nsr/nwab197

[28] Liu C, Bai Y, Li W et al (2022) In situ growth of three-dimensional MXene/metal–organic framework composites for high-performance supercapacitors. Angew Chem Int Ed 61:e202116282. https://doi.org/10.1002/anie.202116282

[29] Shin D-H, Woo S, Yem H et al (2014) A self-reducible and alcohol-soluble copper-based metal-organic decomposition ink for printed electronics. ACS Appl Mater Interfaces 6:3312–3319. https://doi.org/10.1021/am4036306

[30] Li W, Li L, Li F et al (2022) Self-organizing, environmentally stable, and low-cost copper-nickel complex inks for printed flexible electronics. ACS Appl Mater Interfaces 14:8146–8156. https://doi.org/10.1021/acsami.1c21633

[31] Puyo M, Lebon E, Vendier L et al (2020) Topological analysis of Ag–Ag and Ag–N interactions in silver amidinate precursor complexes of silver nanoparticles. Inorg Chem 59:4328–4339. https://doi.org/10.1021/acs.inorgchem.9b03166

[32] Zope KR, Cormier D, Williams SA (2018) Reactive silver oxalate ink composition with enhanced curing conditions for flexible substrates. ACS Appl Mater Interfaces 10:3830–3837. https://doi.org/10.1021/acsami.7b19161

[33] Nakano M, Fujiwara T, Koga N (2016) Thermal decomposition of silver acetate: physico-geometrical kinetic

features and formation of silver nanoparticles. J Phys Chem C 120:8841–8854. https://doi.org/10.1021/acs.jpcc.6b02377

[34] Liu Y, Chen C, Zhang Z et al (2022) Development of crackless and deformation-resistant electroplated Ni/electroless Ni/Pt/Ag metallization layers for Ag-sintered joint during a harsh thermal shock. Mater Des 224:111389. https://doi.org/10.1016/j.matdes.2022.111389

[35] Yang W, Wang C, Arrighi V (2018) An organic silver complex conductive ink using both decomposition and self-reduction mechanisms in film formation. J Mater Sci: Mater Electron 29:2771–2783. https://doi.org/10.1007/s10854-017-8205-7

[36] Fang H, Wang C, Zhou S et al (2020) Rapid pressureless and low-temperature bonding of large-area power chips by sintering two-step activated Ag paste. J Mater Sci: Mater Electron 31:6497–6505. https://doi.org/10.1007/s10854-020-03207-y

[37] Wang C, Zhang X, Zhang Y, et al (2022) Pressureless and low temperature sintering by Ag paste for the high temperature die-attachment in power device packaging. In: 2022 IEEE 72nd Electronic Components and Technology Conference (ECTC). pp 2256–2262. https://doi.org/10.1109/ECTC51906.2022.00356

[38] Paknejad SA, Dumas G, West G et al (2014) Microstructure evolution during 300 °C storage of sintered Ag nanoparticles on Ag and Au substrates. J Alloys Compd 617:994–1001. https://doi.org/10.1016/j.jallcom.2014.08.062

[39] Deng Z, Zou G, Du R et al (2024) Particle size effects of nano-Ag films on the interface sintered bonding for die attachment. J Electron Mater 53:473–488. https://doi.org/10.1007/s11664-023-10786-z

[40] Lange AP, Samanta A, Majidi H et al (2016) Dislocation mediated alignment during metal nanoparticle coalescence. Acta Mater 120:364–378. https://doi.org/10.1016/j.actamat.2016.08.061

[41] Yang H, Zhu W (2020) Study on the main influencing factors of shear strength of nano-silver joints. J Mater Res Technol 9:4133–4138. https://doi.org/10.1016/j.jmrt.2020.02.040

[42] Lu X, Lv Z, Sun Y et al (2022) Enhanced mechanical and thermal properties of Ag joints sintered by spark plasma sintering. J Electron Mater 51:6310–6319. https://doi.org/10.1007/s11664-022-09849-4

[43] Chen S, Mei Y-H, Wang M et al (2022) Large-area bonding by sintering of a resin-free nanosilver paste at ultralow temperature of 180 °C. IEEE Trans Compon Packaging Manuf Technol 12:707–710. https://doi.org/10.1109/TCPMT.2022.3159033

[44] Wang C, Li G, Xu L et al (2021) Low temperature sintered silver nanoflake paste for power device packaging and its anisotropic sintering mechanism. ACS Appl Electron Mater 3:5365–5373. https://doi.org/10.1021/acsaelm.1c00857

[45] Yang D, Huang Y, Tian Y (2021) Microstructure of Ag nano paste joint and its influence on reliability. Crystals 11:1537. https://doi.org/10.3390/cryst11121537

[46] Zhang Z, Chen C, Suetake A et al (2021) Reliability of Ag sinter-joining die attach under harsh thermal cycling and power cycling tests. J Electron Mater 50:6597–6606. https://doi.org/10.1007/s11664-021-09221-y

[47] Yin C, Wumaeraili K, Zhang Y et al (2024) Novel Ag–Cu foam sheet with multi-layer composite structure for high performance joining of SiC power chips. Mater Charact 209:113696. https://doi.org/10.1016/j.matchar.2024.113696

[48] Fang ZZ, Wang H (2013) 13—Sintering of ultrafine and nanosized ceramic and metallic particles. In: Banerjee R, Manna I (eds) Ceramic nanocomposites. Woodhead Publishing, Sawston, pp 431–473

[49] Molinari A (2022) Fundamentals of sintering: solid state sintering. In: Caballero FG (ed) Encyclopedia of materials: metals and alloys. Elsevier, Oxford, pp 471–480

[50] Yan J (2021) A review of sintering-bonding technology using Ag nanoparticles for electronic packaging. Nanomaterials. https://doi.org/10.3390/nano11040927

[51] Zuo Y, Zhao C, Robador A et al (2022) Quasi-in-situ observation of the grain growth and grain boundary movement in sintered Cu nanoparticle interconnects. Acta Mater 236:118135. https://doi.org/10.1016/j.actamat.2022.118135